On the relationship between total differential phase and path-integrated attenuation at X-band in an Alpine environment

Guy Delrieu[1], Anil Kumar Khanal[1], Nan Yu[2], Frédéric Cazenave[1], Brice Boudevillain[1], and Nicolas Gaussiat[2]

1 Institute for Geosciences and Environmental research (IGE), UMR 5001 (Université Grenoble Alpes, CNRS, IRD, Grenoble-INP), Grenoble, France

2 Centre de Météorologie Radar, Direction des Systèmes d'Observation, Météo France, Toulouse, France

Correspondence to: guy.delrieu@univ-grenoble-alpes.fr

Abstract. The RadAlp experiment aims at developing advanced methods for rain and snow estimation using weather radar remote sensing techniques in high mountain regions for improved water resource assessment and hydrological risk mitigation. A unique observation system has been deployed since 2016 in the Grenoble region, France. It is composed of a X-band radar operated by Météo-France on top of the Mt Moucherotte (1970 m asl; MOUC radar hereinafter). In the Grenoble valley (220 m asl), we operate a research X-band radar called XPORT and *in situ* sensors (weather station, rain gauge, disdrometer). We present in this article a methodology for studying the relationship between the total differential phase (ψ_{dp}) and path-integrated attenuation (PIA) at X-Band, a relationship critical for the implementation of attenuation corrections based on polarimetry. We use the Mountain Reference Technique for direct PIA estimations associated with the decrease of returns from mountain targets during precipitation events. The polarimetric PIA estimations are based on the regularization of the ψ_{dp} radial profiles and their derivation in terms of specific differential phase (K_{dp}) profiles, followed by the application of relationships between the specific attenuation and the specific differential phase. Such $k - K_{dp}$ relationships are estimated for rain by using available DSD measurements, empirical oblateness models for raindrops and a scattering model. Two contrasted precipitation events are considered in this preliminary study: (i) a convective case with strong rainrates allows us to study the $\phi_{dp} - PIA$ relationship in rain; (ii) during a stratiform case with moderate rainrates, for which the melting layer (ML) rose up from about 1000 m asl up to 2500 m asl, we were able to perform a horizontal scanning of the ML with the MOUC radar and a detailed analysis of the $\phi_{dp} - PIA$ relationship in the various parts of the ML. The rain case study indicates that the relationship between MRT-derived PIAs and polarimetry-derived PIAs presents a considerable dispersion (explained variance of 0.72) in rain. Interestingly, the non-linear $k - K_{dp}$ relationship derived from independent DSD measurements allows obtaining almost unbiased PIA estimates. For the stratiform case, the averaged PIA/ψ_{dp} ratio peaks within the melting layer at the level of the co-polar correlation coefficient (ρ_{hv}) peak, just below the reflectivity peak, with a value of about 0.4 dB degree[-1]. Its value in

rain below the ML is 0.27 dB degree^{-1}, in very good agreement with the slope of the linear $k - K_{dp}$ relationship derived from DSD measurements at ground level. The PIA/ψ_{dp} ratio remains quite strong in the upper part of the ML, between 0.32 and 0.38 dB degree^{-1}, before tending towards 0 above the ML.

1 Introduction

Estimation of atmospheric precipitation (solid / liquid) is of paramount importance in a mountainous region such as the Alps for the assessment and management of water and snow resources for drinking water, hydro-power production, agriculture and tourism, characterized by high seasonal variability. One of the most critical application concerns the prediction of natural hazards associated with intense precipitation and melting of snowpacks, i.e. inundations, floods, flash floods and gravitational movements, which requires a high-resolution observation: spatial resolution $\leq 1km^2$ and temporal resolution $\leq 1hr$. While this can hardly be achieved with traditional *in-situ* raingauge networks, the use of radar remote sensing has a high potential that needs to be exploited but also a number of limitations that need to be overpassed. Quantitative Precipitation Estimation (QPE) with radar remote sensing in a complex terrain such as the Alps is made challenging by the topography and the space-time structure and dynamics of precipitation systems. Radar coverage of the mountain regions brings the following dilemma. On the one hand, installing a radar at the top of a mountain allows a 360° panoramic view and therefore the ability to detect precipitation systems over a long range at the regional scale. This is particularly relevant for localized and heavy convective systems in warm seasons. But the precipitation is likely to undergo significant change in between detection and arrival at ground level, including a phase change when the 0° C isotherm is located at the level of or lower than the radar elevation. Such situations are likely to be frequent during cold periods, with a strong impact on QPE quality at ground level. On the other hand, installing a radar at the bottom of the valley provides high resolution and quality data required for vulnerable and densely populated Alpine valleys, but the QPEs are limited at the latter due to beam blockage by surrounding mountains.

MeteoSwiss has a long-standing experience in operating its C-band radar network in the Alps (Joss and Lee, 1995; Germann et al. 2006) and at coping with the associated altitude dilemma. In addition to physically-based radar data processing aimed at determining vertical profiles of reflectivity and at taking benefit of polarimetry, sophisticated radar-raingauge merging techniques and echo tracking techniques, as well as numerical prediction models outputs (Sideris et al. 2014; Foresti et al. 2018) are implemented to better understand and quantify the complexity of precipitation distribution in such a rugged environment. More recently, Météo-France has chosen to complement the coverage of its operational radar network ARAMIS (for Application Radar à la Météorologie Infra-Synoptique) in the Alps by means of X-Band polarimetric and Doppler radars. A first set of three radars was installed in Southern Alps within the RHyTMME project (Risques Hydrométéorologiques en Territoires de Montagnes et Méditerranéens) in the period 2008-2013 at Montagne de Maurel (1770 m above sea level, asl), Mont Colombis (1740 m asl) and Vars Mayt (2400 m asl) (Westrelin et al. 2012). This effort has been continued in 2014-2015 with the installation of an additional X-band radar system (MOUC radar, hereinafter) on top of the Mount Moucherotte (1920

m) that dominates the valley of Grenoble, the biggest city in the French Alps with about 500,000 inhabitants. The choice of the X-Band frequency is challenging due to its sensitivity to attenuation (e.g. Delrieu et al. 2000). In the past, the IGE radar team has proposed the so-called Mountain Reference Technique (MRT) (Delrieu et al. 1997; Serrar et al. 2000; Bouilloud et al. 2009) to take advantage of this drawback for both correcting for attenuation and performing a self-calibration of the radar. The idea was to estimate path-integrated attenuations (PIA) in some specific directions from the decrease of mountain returns during rainy periods. Such PIA estimates were then used as constraints for backward or forward attenuation correction algorithms (Marzoug and Amayenc 1994) with optimization of an effective radar calibration error, given a drop size distribution (DSD) parameterization. The development of polarimetric radar techniques (e.g. Bringi and Chandrasakar 2001; Ryzhkov et al. 2005) has allowed a scientific breakthrough for quantitative precipitation estimation (QPE) at X-band by exploiting the relationship which exists between the specific differential phase (K_{dp}, in ° km^{-1}) and the specific attenuation k (dB km^{-1}). Similarly to the MRT, the differential propagation phase $\Phi_{dp}(r_2) - \Phi_{dp}(r_1)$ over a given path (r_1, r_2) can be used to estimate $PIA(r_1, r_2)$, which can be used to constrain a backward attenuation correction algorithm and allow a self-calibration of the radar and/or an adjustment of the DSD parameterization (Testud et al. 2000; Ryzhkov et al. 2014). Two major advantages of the polarimetric technique over the MRT can be formulated: (1) the availability of PIA constraints for any direction with significant precipitation and (2) the subsequent possibility to use a backward attenuation correction algorithm, which is known to be stable while the forward formulation is essentially unstable. Accounting for their respective potential in different rain regimes (moderate to heavy), some combined algorithms making use of various polarimetric observables (reflectivity, differential reflectivity and specific differential phase) have also been proposed for the X-Band frequency (e.g. Matrosov and Clark, 2002; Matrosov et al. 2005; Koffi et al. 2014). Although the polarimetric QPE methodology is now quite well established and validated for rainy precipitation (Matrosov et al., 2005; Anagnostou et al. 2004; Diss et al. 2009), Yu et al. (2018) point out, in their first performance assessment of the RHyTMME radar network, (i) the need to better understand and quantify attenuation effects in the melting layer (ML), (ii) the importance of non-uniform beam filling (NUBF) effects at medium to long ranges in such a high-mountain context, as well as (iii) the stronger impact of radome attenuation at X-band compared to S- or C-Band.

Since 2016, we have the opportunity to operate a research X-Band polarimetric radar system (XPORT radar hereinafter) at IGE at the bottom of the Grenoble valley. This unique facility, consisting of two radar systems 11 km apart operating on an altitudinal gradient of about 1700 m, should enable us to make progress on how to deal with the altitude dilemma and with potential / issues associated with the choice of the X-band operating frequency. Following a first article based on the RadAlp experiment about the characterization of the melting layer (Khanal et al. 2019), we concentrate hereinafter on the relationship between total differential phase (ϕ_{dp}) derived from polarimetry and PIA derived from the MRT. In section 2, we present the observation system available, as well as the two contrasted rainy events considered in this study: (i) a convective case with strong rainrates, for which the melting layer was well above the detection domain of the XPORT radar, allows us to study the $\phi_{dp} - PIA$ relationship in rain; (ii) during a stratiform case with moderate rainrates, for which the melting layer rose up from

about 1000 m asl up to 2500 m asl, we were able to perform a horizontal scanning of the ML with the MOUC radar and a detailed analysis of the $\phi_{dp} - PIA$ relationship in the various layers of the ML. We present and illustrate in section 3 the methodology used for the PIA and ϕ_{dp} estimation. We also investigate in section 3 the relationship between the specific differential phase (K_{dp}) and the specific attenuation (k) thanks to drop size distribution (DSD) measurements collected in the Grenoble valley during the two events. The results concerning the $\phi_{dp} - PIA$ relationship in rain and in the ML are presented and discussed in section 4, while conclusions and perspectives are drawn in section 5.

2. Observation system and datasets

2.1. Observation system

Grenoble is a Y-shaped alluvial valley in the French Alps with a mean altitude of about 220 m asl surrounded by three mountain ranges: Chartreuse (culminating at 2083 m asl) to the north, Belledonne (2977 m) to the south-east and Vercors (2307 m) to the west. Figure 1 shows the topography of the area as well as the positions of the Météo-France radar system on top of the Mt Moucherotte and the IGE experimental site at the bottom of the valley.

Figure 1 here

Among other devices, the IGE experimental site includes: (i) the IGE XPORT research radar [13], see Table 1 for the list of its main parameters; (ii) one micro-rain radar (MRR, not used in the current study, (iii) one meteorological station including pressure, temperature, humidity, wind probes and several raingauges, (iv) one PARSIVEL2 disdrometer. The characteristics of the MOUC radar are listed in Table 1 as well. XPORT radar was constructed in the laboratory in the 2000s. It was operated during more than 10 years in Western Africa within the AMMA and Megha Tropiques Cal-Val campaigns. Since its return in France in 2016, a maintenance and updating program is underway to improve its functionalities, notably with respect to the real time data processing and the antenna control program. One noticeable feature for XPORT radar is the range bin size of 33 m (corresponding actually to an over-sampling since, for a pulse width of 1 µs, the theoretical bin size is 150 m) which is an interesting figure for the close range and volumic measurements considered in this study. Note that while the MOUC radar is operated 24 hours a day and its data integrated in the Météo France mosaic radar products, the XPORT radar is operated on alerts only for significant precipitation events.

2.2 Dataset

Figure 2 gives presents the two contrasted rain events considered in this study. In both cases, the total rain amount observed at the IGE site was about 35 mm, but in 3 hours with two peak rainrates of about 40 mm h⁻¹ for the July 21, 2017 convective event while the January 3-4, 2018 stratiform event lasted more than 12 hours with an average rainrate of about 3 mm h⁻¹. The two events also differ by their vertical structure. The bottom graphs of Fig. 2 display the time series of the altitudes of the tops, peaks and bottoms of the horizontal reflectivity (Zh) and co-polar correlation coefficient (ρ_{hv}) signatures of the ML, derived

from the automatic detection algorithm described in Khanal et al. (2019). The quasi-vertical profiles (Ryzhkov et al. 2016) derived from the XPORT 25°-PPIs are considered in the ML detection. For the convective case, the melting layer extends from 3000 up to 4000 m asl and more, i.e. well above the altitudes of the two radars. For the stratiform event, the ML extends between 800 and 1500 m asl during the first part of the event (between January 3 20:00 UTC to January 4 01:30 UTC) and

130   then rises in about 2 hours to stabilize at an altitude range of about 2200-2800 m asl after 04:00 UTC, passing progressively at the level of the MOUC radar in the meantime.

Figure 2 here

In the following, we will consider the XPORT radar measurements at the elevation angle of 7.5° and the MOUC radar

135   measurements at the elevation angle of 0° to study the $\phi_{dp} - PIA$ relationship in rain and in the ML, respectively.

As an additional illustration of the dataset, Fig. 3 gives two examples of XPORT PPIs at 7.5° elevation angle for moderate (left) and intense (right) rain during the July 21, 2017 event. As a clear feature, one can see that, for this elevation angle, the radar beam is fully blocked by the Chartreuse mountain range in the northern sector. Also visible in the north-east sector and,

140   to a lesser extent, in the south-west sector are the partial beam blockages associated with tall trees in the vicinity of the XPORT radar on the Grenoble campus. This figure is mostly intended to draw the attention of the reader on the decrease on the Chamrousse and Moucherotte mountain returns (within red circles) during the intense rain time step compared to their values in moderate rain, as a first illustration of the MRT principle.

145   *Figure 3 here*

3. Methodology

3.1. Path-integrated attenuation and differential propagation phase estimation

Our aim is to study the relationship between two radar observables of propagation effects at X-Band: path-integrated

150   attenuation and differential propagation phase due to precipitation occurring along the radar path.

Let us express the PIA (in dB) at a given range r (km) as:

$$PIA(r) = PIA(r_0) + 2 \int_{r_0}^{r} k(s) \, ds \qquad (1)$$

where $k(s)$ (dB km^{-1}) is the specific attenuation due to rain at range s (km). r_0 is the range where the measurements start to become exploitable, i.e. the range where measurements are free of ground clutter associated with side lobe effects. The term

155    $PIA(r_0)$ represents the so-called on-site attenuation resulting from radome attenuation and range attenuation at range closer than r_0. Delrieu et al. (1999) have proposed an assessment of the quality of PIA estimates from mountain returns by

implementing a receiving antenna in the Belledonne mountain range in conjunction with an X-band radar operated on the
Grenoble campus. Basically, they found a good agreement between the two PIA estimates for PIAs exceeding the natural
variability of the mountain reference target during dry weather. They recommended using strong mountain returns (greater

160   than e.g. 50 dBZ during dry weather) so as to minimize the impact of precipitation falling over the reference target itself. They
also point out that this approach is not able to separate the effects of on-site and range attenuation. They verified however, by
implementing the receiving antenna close to the radar (at a range of about 200 m), that the on-site attenuation was negligible
for a radomeless radar, which is the case for the XPORT radar but not for the MOUC radar. Another interesting feature of the
MRT PIA estimator is its independence with respect to eventual radar calibration errors.

165   Now, let us express the differential propagation phase between co-polar (hh and vv) received signals as:

$$\psi_{dp}(r) = 2 \int_{r_0}^{r} K_{dp}(s)\, ds + \delta_{hv}(r) \tag{2}$$

where $K_{dp}(s)$ is the specific differential phase [° km^{-1}] related to precipitation at any range s between r_0 and r, and $\delta_{hv}(r)$ is
the differential phase upon scattering [°] at range r.

The quantity of interest, the differential propagation phase associated with precipitation along the path, is denoted:

170    $$\phi_{dp}(r) = 2 \int_{r_0}^{r} K_{dp}(s)\, ds = \psi_{dp}(r) - \delta_{hv}(r) \tag{3}$$

Like with the on-site attenuation for the MRT technique, we have here a problem with the possible influence of the differential
phase upon scattering $\delta_{hv}(r)$ that may introduce a positive bias on the estimation of the differential propagation phase
associated with precipitation along the path. We find in the literature (e.g. Otto and Russenberg 2011; Schneebeli and Berne
2012) power-law relationships between δ_{hv} and Z_{dr} at X-band in rain, giving values for backscattering phase shift in the

175   ranges of [0.6 – 1.0] and [2.1 – 3.5] for differential reflectivity of 1 and 2 dB, respectively. Scattering simulations based on
disdrometer data (Trömel et al. 2013) indicate that there is quite a large scatter with respect to such power-law models and an
important influence of the considered hydrometeor temperature. Keeping this problem and the related orders of magnitude in
mind, we will consider in this preliminary study ψ_{dp} to be an estimator of ϕ_{dp}. In other words we will suppose δ_{hv} to be
negligible with respect to ϕ_{dp}.

180   Other difficulties in the ϕ_{dp} estimation are in identifying the system differential phase and in dealing with the noise affecting
the ψ_{dp} measurements. The system differential phase was estimated by the median value of the raw ψ_{dp} profile over the N
closest rainy rain gates (see below for the determination of the rainy range gates), with $N=10$ for XPORT radar, i.e. a range
extent of 330 m and $N=4$ for MOUC radar, i.e. a range extent of 960 m. Regarding the ψ_{dp} measurement noise, we have
implemented a regularization procedure proposed by Yu and Gaussiat (2018) which consists in defining an upper envelope

185   curve and a lower envelope curve of the measured ψ_{dp} profile that are progressively brought together by an iterative

elimination of anomalous ψ_{dp} jumps from one range gate to the next. In a final step, the regularized ψ_{dp} profile (increasing monotonous curve) is estimated by taking the average of the upper and lower envelope curves. Such an algorithm may be efficient to some extent to filter nonmonotonic behaviour of the ψ_{dp} profile associated with contribution from δ_{hv}.

For both the PIA and ψ_{dp} estimators, it was found necessary to determine so-called rainy range gates along the path, especially
190 to determine the r_0 value and a range value close to the reference target, denoted r_M, for which the ψ_{dp} values are not affected by mountain clutter. For this purpose, we considered a given range gate as rainy if $Z_h \geq 15\ dBZ$ and $\rho_{hv} \geq 0.95$ for rain profiles. We had to suppress the ρ_{hv} constraint for profiles passing through the melting layer, due to the well-known decrease of ρ_{hv} in the ML (Khanal et al. 2019).

Figure 4 illustrates the PIA and ϕ_{dp} estimation method for a given mountain target for the measurements of the 7.5° PPI of
195 the XPORT radar for two time steps during the convective event of July 21, 2017. The selected target at range 14 km (top graph) comprises a series of successive gates with dry-weather mean reflectivity value greater than 45 dBZ. The raw reflectivity profiles exhibit a decrease of about 5 and 20 dB compared to the dry-weather returns at the reference target range. The measured ψ_{dp} profiles (middle) are comparatively noisier in weak precipitation. The regularization procedure is illustrated with the display of the two envelope curves. The resulting increasing monotonous curves provide good fits to the
200 raw profiles, with ψ_{dp} estimates of 12 and 60° near the reference mountain target for the two examples. The ρ_{hv} profiles (bottom graphs) confirm that rain is present on the entire profiles and they allow to detect clutter at close range and for the mountain reference target. Note that the ρ_{hv} perturbations in the region of the mountain target are less pronounced for the case with more intense precipitation (right), probably as the result of heavier rain falling over the mountain itself.

Figure 4 here
205

Figure 5 provides another illustration of the methodology with the time series of (a) the apparent reflectivity of a given mountain target, (b) the resulting PIA estimates, and (c) the $\psi_{dp}(r_M)$ estimates for the 0°-PPI of the MOUC radar during the stratiform event of January 3-4, 2018. The time period considered in the figure ranges from 00:00 UTC to 06:00 UTC on January 4th, 2018 in order to focus on the rising of the ML between 02:00 UTC and 04:00 UTC. The considered target
210 is located at distances comprised between 26.4 and 29.7 km from the radar. The bottom plot (d) of Fig. 5 displays the results of the ML detection algorithm (Khanal et al. 2019) in terms of the altitudes of the top, peak and bottom of the Z_h (blue) and the ρ_{hv} (orange) ML signatures. The altitude of the Z_h top inflexion point is assumed to correspond to the 0°C isotherm altitude while the ρ_{hv} bottom inflexion point corresponds well with the bottom of the ML according to Khanal et al. (2019). We therefore define the ML width as the altitude difference between Zh top and ρ_{hv} bottom.

215 Before 02:00 UTC, the ML is well below the altitude of the MOUC radar. MOUC radar measurements at the 0°-elevation angle are therefore made in snow/ice precipitation during this period. Based on the ML detection results, the passage of the

ML at the altitude of the MOUC radar begins at about 02:20 UTC and ends at 04:10 UTC. After this time, MOUC radar measurements are therefore made in rainfall. Assuming attenuation at X-band to be negligible in snow, we consider the average of the apparent reflectivity of the mountain reference target between 00:00 UTC and 02:00 UTC (horizontal red line in Fig. 5a) as the dry-weather reference value required for our PIA estimations. During this period, the PIA is subsequently set to 0. The mean value of $\psi_{dp}(r_M)$ is equal to 12.3°, resulting in a specific differential phase of 0.22 °km^{-1} if the differential phase upon scattering is neglected. Such values indicate a significant heterogeneity of the horizontal and vertical dimensions of the snow/ice hydrometeors.

Figure 5 here

225

During the other two periods, the PIA is simply estimated as the difference between the dry-weather reference value and the apparent reflectivity of the mountain target at the considered time step. Note that a slightly more sophisticated method has been proposed in [7] to determine the dry-weather base line by considering the reference target reflectivity before and after precipitation, in an attempt to account for possible effects of the wetting of the mountain surfaces. The reference mountain returns do not exhibit significant differences before and after precipitation (not shown in Fig. 5 since we concentrate on the period of ML rising), which justifies the simple method used in this study. During the rainy period after 04:10 UTC, the average PIA is 3.3 dB, corresponding to an average specific attenuation of 0.059 dB km^{-1}. This estimate is rather high (overestimation of 37%) if compared with the specific attenuation estimate derived from the $k - R$ relationship proposed by Delrieu et al. (1991) for widespread rainfall at X-Band for a temperature of 0°C: $k = 1.05\ 10^{-2}\ R^{1.15}$. This empirical relationship yields $k = 0.037$ dB km^{-1} for $R = 3$ mm h^{-1}; the latter value being the average rainrate observed at the IGE site between 04:00 UTC and 06:00 UTC. The average $\psi_{dp}(r_M)$ value during the same period is 9.7°, corresponding to a mean K_{dp} value of 0.173 °km^{-1} if the differential phase upon scattering is neglected. Using the $k - K_{dp}$ relationship established for this event by using the DSD measurements available at the IGE site (see section 3.2 below), one obtains a k value of 0.036 dB km^{-1}, in remarkable agreement with the k estimate derived from the $k - R$ relationship for widespread rainfall. These simple calculations have to be considered with caution. However, they suggest a slight PIA overestimation of about 1 dB during the rainy period, which could be well associated with radome attenuation of the MOUC radar.

Our main objective with the January 3-4, 2018 event is to study the $\phi_{dp} - PIA$ relationship within the ML. Figure 5 clearly indicates that both variables take, as expected, higher values during that period compared to during the snow and the rainy periods. The maximum values reached are 13.1 dB for PIA and 23.0° for $\psi_{dp}(r_M)$. Figures 5b and 5c also show that the co-fluctuation of the two time series is not that good during the ML period with a $\psi_{dp}(r_M)$ signal having a trapezoidal shape with maximum values between 02:35 UTC and 03:15 UTC while the PIA signal is more triangular and peaks at 03:15 UTC. We note that the two signals compare well after the peak and that they both peak down at around 04:00 UTC when measurements are made in the lowest part of the ML. These features are quite systematic for all the sixteen targets considered for the MOUC

radar for this event, giving the impression that the $\phi_{dp} - PIA$ relationship depends on the position within the ML and as such
250 on the physical processes occurring during the melting. This point will be further illustrated and discussed in sub-section 4.2.

3.2. Study of the k $-$ K$_{dp}$ relationship in rain from in-situ DSD measurements

Before presenting the analysis of the $\phi_{dp} - PIA$ relationship in rain and in the melting layer based on the estimates for all
the mountain targets and time steps available for the two events, we study in this sub-section the $k - K_{dp}$ relationships that
255 we were able to derive from the DSD measurements collected at ground level at the IGE site. For both events, precipitation
was in the form of rainfall at this altitude. As for the scattering model, we used the CANTMAT version 1.2 software
programme that was developed at Colorado State University by C. Tang and V.N. Bringi. The raw PARSIVEL2 DSD
measurements have a time resolution of 1 min. The volumetric concentrations were computed with a 5-min resolution and
binned into 32 diameter classes with increasing sizes from 0.125 mm up to 6 mm. The CANTMAT software uses the T-
260 Matrix formulation to compute radar observables such as horizontal reflectivity, vertical reflectivity, differential reflectivity,
co-polar cross-correlation, specific attenuation, specific phase shift, etc, as a function of the DSD, the radar frequency, air
temperature, oblateness models (e.g. Beard and Chuang 1987; Andsager et al. 1999; Thurai and Bringi 2005) and canting
models for the rain drops as well as the incidence angle of the electromagnetic waves. Figure 6 displays the empirical $k -$
K_{dp} pairs of points obtained for the two events as well as the fits of least-square linear models and power-law non-linear
265 regressions.

Figure 6 here

Based on the literature review mentioning an almost linear relationship between k and K_{dp} at X-Band (Bringi and
270 Chandrasakar, 2001; Testud et al. 2000; Schneebeli and Berne 2012) we have first tested a linear regression with an intercept
forced to be equal to 0 (red line in Fig. 6). This simple model indeed provides a rather good fit to the data, especially for the
convective event. Due to the observed bending of the scatterplots, we have also tested a non-linear regression to a power-law
model (blue curve) which significantly improves the fittings. A sensitivity analysis was performed in order to test the influence
of the raindrop temperature, the raindrop oblateness model, the standard deviation of the canting angle distribution, the
275 incidence angle. For reasonable ranges of variation of these parameters, the DSD itself appears to be the most influent factor
on the values of the regression coefficients. We note that the slopes of our 0-forced linear models are significantly higher than
values proposed in the literature (0.233 in [10]; 0.205 – 0.245 in [19]). The exponents of the fitted power-law models are also
significantly higher than 1.0. The fits in Fig. 6 correspond to the most likely parameterization of the scattering model in terms
of temperature and incidence angles for the two events, i.e. 20°C and 7.5° for the convective case and 0°C and 0° for the
280 stratiform case. The Beard and Chuang (1987) formulation was used as the raindrop oblateness model.

4. Results

4.1. Study of the $\psi_{dp} - PIA$ relationship in rain

285

Figure 7 displays the scatterplot of the $\psi_{dp} - PIA$ values obtained for the July 21st, 2017 convective event with the XPORT 7.5°-PPI data, following the methodology described in section 3.1. The data from sixteen mountain targets, situated between 4 and 16 km from the XPORT radar, were considered. We took care to discard targets leading to receiver saturation at closer ranges. Pairs of points for which MRT PIA estimates were less than 1 dB were discarded as well to account for the temporal

290 variability of the dry-weather mountain returns. This threshold can be seen as a sensitivity limit of the MRT PIA estimator. Since we consider the two variables on an equal footing, we preferred to calculate the least-rectangles regression (blue straight line) between the two variables rather than the least-squares regression of one variable over the other one. One can notice the rather large dispersion of the scatterplot, with explained variance of 72%. Quite remarkably, the regression slope (0.44) is relatively close to the $k - K_{dp}$ linear relationship (0.353), reported as the red straight line in Fig. 7.

295

Figure 7 here

To go further, Fig. 8 presents the comparison of the MRT-derived PIAs with the polarimetry-derived PIAs. For the latter, we simply calculated the derivative of the XPORT ψ_{dp} profiles and applied the $k - K_{dp}$ relationships derived from disdrometer

300 measurements (Fig. 6 left). No attempt was made to correct the ψ_{dp} profiles for effect of the differential phase upon scattering, i.e. we assume $\phi_{dp} = \psi_{dp}$. As one could guess from examination of Fig. 7, the linear $k - K_{dp}$ relationship leads to a significant positive bias for the polarimetry-derived PIAs with a least-rectangles slope of 1.29. The non-linear $k - K_{dp}$ relationship does indeed a good job in reducing this bias (least-rectangles slope of 1.05).

305 *Figure 8 here*

4.2. Study of the $\psi_{dp} - PIA$ relationship in the Melting Layer

Figure 9 displays the scatterplot of the $\psi_{dp} - PIA$ values obtained for the January 4th, 2018 stratiform event with the MOUC

310 0°-PPI data, following the methodology described in section 3.1. The data from sixteen mountain targets, situated between 8 and 42 km from the MOUC radar, were considered. Note that a majority of them are located between 22 and 30 km. Here again a 1dB threshold was taken into account as the sensitivity limit of the MRT PIA estimator. One can see that the correlation between the two variables is severely degraded compared to the rain case with an explained variance of 0.41, a least-rectangle

slope of 0.68 dB degree^{-1} and an intercept of -6.44 dB. The red line is the $k - K_{dp}$ linear regression determined with the DSD

315   observed at ground level for this event (Fig. 6 right). Clearly, the $\psi_{dp} - PIA$ relationship is different in rain and in the ML,

and as suggested when commenting Fig. 5, it likely depends on the physical processes occurring during the melting.

Figure 9 here

320   To investigate this point, the $\psi_{dp}(t)$ and $PIA(t)$ values estimated at a given time t are represented in Fig. 10 as a function of

their position within the ML. As already noted, we define the ML width as the difference between the Zh top altitude and the

ρ_{hv} bottom altitude (Khanal et al. 2019). Since the ML width significantly varies during the considered period (from 630 to

1020 m; see Fig. 5), we found necessary to scale the altitudes by the ML width. This was achieved by considering the following

linear transformation of the altitudes:

325

$$H(t) = (h_M - h_{\rho hvB}(t))/MLw(t) \tag{4}$$

where h_M is the altitude [m asl] of the MOUC radar, $h_{\rho hvB}(t)$ is the altitude of the ML bottom at time t and $MLw(t)$ is the

ML thickness at time t. The scaled altitude $H(t)$ [-] subsequently takes the value 0 at ML bottom and the value 1 at ML top

330   (orange and blue thick horizontal lines, respectively, in Fig. 10). Furthermore, in order to locate more precisely the position of

the Zh and ρ_{hv} peaks within the ML, we computed their scaled altitudes at each time step, $H_{zhP}(t)$ and $H_{\rho hvP}(t)$ respectively,

as:

$$H_{zhP}(t) = (h_{zhP}(t) - h_{\rho hvB}(t))/MLw(t) \tag{5}$$

335   and:

$$H_{\rho hvP}(t) = (h_{\rho hvP}(t) - h_{\rho hvB}(t))/MLw(t) \tag{6}$$

where $h_{zhP}(t)$ and $h_{\rho hvP}(t)$ are the altitudes of Zh peak and ρ_{hv} peak at time t. The dotted horizontal lines in Fig. 10 represent

the 10 and 90% quantiles of the timeseries of the scaled altitudes of Zh peak (dotted blue lines) and ρ_{hv} peak (dotted orange

340   lines). We can observe a shift between the Zh and ρ_{hv} characteristic altitudes, consistent with the ML climatology established

by Khanal et al. (2019) who reported a shift of about 100 m in average between the two peaks. We note in Fig. 5 that this shift

is visible before 02:00 UTC but that it is less pronounced during the ML rising and its stabilization after 04:00 UTC. In order

to better evidence their vertical trends, the $PIA(t) - H(t)$ and $\psi_{dp}(t) - H(t)$ points are presented in Fig. 10 in the form of

box plots with an altitude class of size 0.1. The number of counts in each class is indicated on the right of the graphs; it is a

345   multiple of the number of MRT targets (16 here). One can note that the vertical sampling is not very rich, with missing classes

within the ML. However the trends already evoked when commenting Fig.5 are confirmed: (i) the PIA values peak when

measurements are made at the level of the Zh and ρ_{hv} peaks; more precisely, the PIA peak is observed for the altitude class containing the ρ_{hv} peaks ($0.35 - 0.45$); (ii) the region with maximum values is somewhat thicker for ψ_{dp}, encompassing a significant part of the upper ML, between 0.3 and 0.8 in terms of scaled altitudes; (iii) the PIA tends towards its value in rain

350 below the ML and towards 0 above the ML; (iv) ψ_{dp} tends towards almost similar values in average in rain (ML bottom) and snow (ML top).

Finally, Figure 11 displays the evolution of the ratio PIA/ψ_{dp} as a function of the scaled altitudes. The value of the ratio below the ML (0.27) is in remarkable agreement with the slope of the linear model established between the specific attenuation k and

355 the specific differential phase K_{dp} using the DSD measurements in rain available for this event (0.29; see Fig. 6 right). The ratio linearly increases up to the ρ_{hv} peak where it takes a value close to 0.4. For the three classes of scaled altitude 0.7, 0.8 and 0.9, the ratio is between 0.32 and 0.38, with an apparent secondary maximum for the altitude class 0.8. Data with increased vertical resolution would be necessary to confirm or not this result, which is also visible on the PIA profile and on several $\psi_{dp}(t)$ and $PIA(t)$ timeseries like the ones displayed in Fig. 5. Above the ML, the ratio progressively tends toward 0 in about

360 300 to 400 m.

Figure 11 here

5. Summary and conclusions

365

We developed in this work a methodology for studying the relationship between total differential phase (ψ_{dp}) and path-integrated attenuation (PIA) at X-Band. Knowledge of this relationship is critical for the implementation of attenuation corrections based on polarimetry. We used the Mountain Reference Technique for direct PIA estimations associated with the decrease of returns from mountain targets during precipitation events. The polarimetry PIA estimation is based on the

370 regularization of the ψ_{dp} profiles and their derivation in terms of specific differential phase (K_{dp}) profiles followed by the application of a power-law relationship between the specific attenuation and the specific differential phase. Such $k - K_{dp}$ relationship can be evaluated for rain with a scattering model by using DSD measurements and an oblateness model for raindrops.

375 The rain case study for the convective storm of July 21st, 2017 indicates that the relationship between MRT-derived PIAs and polarimetry-derived PIAs presents a considerable dispersion (explained variance of 0.72). Both methods are prone to specific errors and, even if the MRT PIA estimator is more directly related to power attenuation, it is *a priori* difficult to say which estimator is the best. In this preliminary study, we did neglect the possible impact of the differential phase upon scattering $\delta_{hv}(r)$. We remind the reader that the observed PIA range is 1-30 dB while the theoretical δ_{hv} range is 0-3 dB. The δ_{hv} effect

380   may therefore impact the results obtained only at the margin. Similarly, we assumed the on-site attenuation to be negligible
for the MRT PIA estimation, and we are confident that this is true since the XPORT radar is radomeless. In addition, NUBF
effects constitute a third source of error which, although the rain event was convective, should remain limited due to the short
ranges considered and the fact that the ML was well above the observed area. These errors on both PIA estimators will of
course impact the quality of the attenuation corrections and the subsequent QPEs. An assessment exercise with respect to an

385   independent data source (e.g. raingauge measurements) is desirable to distinguish the two PIA estimators. It is however
interesting and encouraging to note that the non-linear $k - K_{dp}$ relationship derived from (independent) DSD measurements
taken during the event of interest at ground level allows a satisfactory transformation of the XPORT ψ_{dp} profiles into almost
unbiased (although dispersed) PIA estimates.

390   The Melting Layer case study of January 3-4th 2018 was made possible by the unique configuration of the observation system
available. The XPORT radar located at the bottom of the valley allowed a fine temporal tracking of the melting layer from
below using quasi-vertical profiles derived from 25°-PPIs. The MOUC radar provided horizontal scans at a higher altitude in
direction of several mountain targets during the rising of the ML in about 2 hours. From this dataset, it was possible to derive
the evolution of $PIA(t, r_M)$, $\psi_{dp}(t, r_M)$, and their ratio, as a proxy for the slope of a linear $k - K_{dp}$ relationship during the

395   ML rising and for a number of mountain targets, as a function of the altitude. Since the ML width varies during the ML rising,
we found necessary to scale the altitudes with respect to the ML width. The three variables considered present a clear signature
as a function of the scaled altitude shown in Figs 10 and 11. In particular, the PIA/ψ_{dp} ratio peaks at the level of the ρ_{hv} peak
(somewhat lower than the Zh peak), with a value of about 0.4 dB degree[-1], while its value in rain just below the ML is 0.27 dB
degree[-1]. The latter value is consistent with the linear $k - K_{dp}$ relationship established from concomitant DSD measurements

400   at ground level. The PIA/ψ_{dp} ratio remains quite strong in the upper part of the ML, between 0.32 and 0.38 dB degree[-1],
before tending towards 0 above the ML. Although the MOUC measurements were made with a 0° elevation angle, NUBF
effects probably introduce some smoothing, variable as a function of the range of the considered mountain targets: with its 3-
dB beamwidth of 1.28°, we remind the vertical resolution of the measurements of the MOUC radar to be for instance of 446
m at 20 km. The δ_{hv} effect is likely to be more influent in this case compared to the rain case since the PIA range is significantly

405   lower, with maximum PIAs of 15 dB. Radome attenuation may also affect the MRT PIA estimates during the ML rising. This
effect may remain limited due to the weak rainrates observed during this event (3 mmh[-1] at the IGE site).

The preliminary results presented in this article will be extended thanks to the datasets collected between 2016 and now, with
a wider variety of precipitation events, as well as with physically-based simulations. It is in particular important to assess to

410   which extent the XPORT volumetric measurements are affected by attenuation in moderate precipitation leading to well
defined ML layers, when the ML is below or at the level of the MOUC radar. These are indeed the situations for which we
expect the main added-value of the down-valley observations made at IGE.

Acknowledgements

415   We are grateful to P.N. Gatlin (NASA Marshall Space Flight Center, Huntsville, AL) for providing the CANTMAT version
1.2 software developed at Colorado State University by C. Tang and V.N. Bringi, who we also thank. The RadAlp experiment
is co-funded by the Labex osug@2020, the Service Central Hydrométéorologique et d'Appui à la Prévision des Inondations
(SCHAPI) and Electricité de France / Division Technique Générale (EDF/DTG).

References

420   Anagnostou, E.N., Anagnostou, M.N., Krajewski, W.F., Kruger, A., and Miriovsky, B.J.: High-Resolution Rainfall
Estimation from X-Band Polarimetric Radar Measurements. J. Hydrometeor., 5, 110–128. https://doi.org/10.1175/1525-
7541(2004)005<0110:HREFXP>2.0.CO;2, 2004.

Beard, K.V., and Chuang, C.: A new model for the equilibrium shape of raindrops, J. Atmos. Sci., 44, 1509-1524.
425   https://doi.org/10.1175/1520-0469(1987)044<1509:ANMFTE>2.0.CO;2, 1987.

Andsager, K., Beard, K.V., and Laird, N.E.: Laboratory measurements of axis ratios for large raindrops. J. Atmos. Sci., 56,
2673-2683. https://doi.org/10.1175/1520-0469(1999)056<2673:LMOARF>2.0.CO;2, 1999.

430   Bouilloud, L., Delrieu, G., Boudevillain, B., Borga, M., and Zanon, F.: Radar rainfall estimation for the post-event analysis
of a Slovenian flash-flood case: application of the Mountain Reference Technique at C-band frequency. Hydrol. Earth Syst.
Sci. 13(7): 1349-1360. DOI: 10.5194/hessd-6-667-2009, 2009.

Bringi, V.N., and Chandrasekar, V.: Polarimetric Doppler weather radar, principles and applications. Cambridge University
435   Press, 636 pp, 2001.

Delrieu, G., Creutin, J.D., and Saint-Andre, I.: Mean K-R Relationships: Practical Results for Typical Weather Radar
Wavelengths. J. Atmos. Oceanic Technol., 8, 467–476, https://doi.org/10.1175/1520-
0426(1991)008<0467:MRRPRF>2.0.CO;2, 1991.
440
Delrieu, G., Serrar, S., Guardo, E., and Creutin, J.D.: Rain Measurement in Hilly Terrain with X-Band Weather Radar
Systems: Accuracy of Path-Integrated Attenuation Estimates Derived from Mountain Returns. J. Atmos. Oceanic Technol.,
16, 405–416, https://doi.org/10.1175/1520-0426(1999)016<0405:RMIHTW>2.0.CO;2, 1999.

445   Delrieu, G., Andrieu, H., and Creutin, J.D.: Quantification of path-integrated attenuation for X- and C-band weather radar
systems operating in Mediterranean heavy rainfall. J. Appl. Meteor. , 39(6), 840-850.
http://dx.doi.org/10.1175/1520-0450(2000)039%3C0840:QOPIAF%3E2.0.CO;2, 2000.

Diss, S., Testud, J., Lavabre, J., Ribstein, P., Moreau, E., and Parent du Chatelet, J.: Ability of a dual polarized X-band radar
450   to estimate rainfall, Advances in Water Resources, 32(7), 975-985, https://doi.org/10.1016/j.advwatres.2009.01.004, 2009.

Foresti, L., Sideris, I.V., Panziera, L., Nerini, D., and Germann, U.: A 10-year radar-based analysis of orographic
precipitation growth and decay patterns over the Swiss Alpine region. Q. J. R. Meteorol. Soc., 144(176), 2277-2301, DOI:
10.1002/qj.3364, 2018.
455

Germann, U., Galli, G., Boscacci, M., and Bolliger, M.: Radar precipitation measurement in a mountainous region. Q. J. Royal Meteorol. Soc., 132(618), 1669-1692; DOI: 10.1256/qj.05.190, 2006.

Joss, J. and Lee, R.: The Application of Radar-Gauge Comparisons to Operational Precipitation Profile Corrections. J. Appl. Meteor., 34, 2612–2630, http://dx.doi.org/10.1175/1520-0450(1995)034<2612:TAORCT>2.0.CO;2, 1995.

Khanal, A. K., Delrieu, G., Cazenave, F., and Boudevillain, B.: Radar remote sensing of precipitation in high mountains: detection and characterization of Melting Layer in French Alps, Atmosphere, 10, 784; doi:10.3390/atmos10120784, 2019.

Koffi, A.K, Gosset, M., Zahiri, E.-P., Ochou, A.D., Kacou, M., Cazenave, F., and Assamoi, P.: Evaluation of X-band polarimetric radar estimation of rainfall and rain drop size distribution parameters in West Africa. Atmospheric Research, 143, 438-461. DOI:10.1016/j.atmosres.2014.03.009, 2014.

Marzoug, M., and Amayenc, P.: A class of single and dual-frequency algorithms for rain-rate profiling from a spaceborne radar: Part 1- Principle and tests from numerical simulations. J. Atmos. Oceanic Technol., **11**, 1480-1506. http://dx.doi.org/10.1175/1520-0426(1994)011%3C1480:ACOSAD%3E2.0.CO;2, 1994.

Matrosov, S. Y., and Clark, K.A.: X-Band Polarimetric Radar Measurements of Rainfall. J. Appl. Meteor. 41(9): 941-952. http://dx.doi.org/10.1175/1520-0450(2002)041%3C0941:XBPRMO%3E2.0.CO;2, 2002.

Matrosov, S.Y., Kingsmill, D.E., Martner, B.E., and Ralph, F.M.: The Utility of X-Band Polarimetric Radar for Quantitative Estimates of Rainfall Parameters. J. Hydrometeor., **6**, 248–262, https://doi.org/10.1175/JHM424.1, 2005.

Otto, T., and Russchenberg, H.W.J.: Estimation of Specific Differential Phase and Differential Backscatter Phase From Polarimetric Weather Radar Measurements of Rain, IEEE Geoscience and Remote Sensing Letters, Vol8, Issue5, 988-992, DOI: 10.1109/LGRS.2011.2145354, 2011.

Ryzhkov, A.V., Giangrande, S.E., and Schuur, T.J.: Rainfall estimation with a polarimetric prototype of WSR-88D.J. Appl. Meteor., Vol. 44, Issue 4, p502-515. DOI: 10.1175/JAM2213.1, 2005.

Ryzhkov, A. V., Diederich, M., Zhang Pengfei, and Simmer, C.: Potential utilization of specific attenuation for rainfall estimation, mitigation of partial beam blockage and radar networking. J. Atmos. Oceanic Technol., Vol. 31, p599-619. DOI: 10.1175/JTECH-D-15-00038.1, 2014.

Ryzhkov, A., Zhang, P., Reeves, H., Kumjian, M., Tschallener, T., Trömel, S., and Simmer, C.: Quasi-Vertical Profiles—A new way to look at polarimetric radar data. J. Atmos. Ocean. Technol., 33, 551–562. doi:10.1175/JTECH-D-15-0020.1, 2016.

Schneebeli, M., and Berne, A.: An Extended Kalman Filter Framework for Polarimetric X-Band Weather Radar Data Processing. J. Atmos. Oceanic Technol., 29, 711–730, https://doi.org/10.1175/JTECH-D-10-05053.1, 2012.

Serrar, S., Delrieu, G., Creutin, J.D., Uijlenhoet, and R.: Mountain Reference Technique: Use of mountain returns to calibrate weather radars operating at attenuating wavelengths. J. Geophys. Res. – Atmospheres, 105(D2): 2281-2290. DOI :10.1029/1999JD901025, 2000.

Sideris, I. V., Gabella, M., Erdin, R., and Germann, U.: Real-time radar–raingauge merging using spatio-temporal co-kriging with external drift in the alpine terrain of Switzerland. Q. J. R. Meteorol. Soc., 140, 1097 – 1111, DOI:10.1002/qj.2188S, 2014.

505 Testud, J, Le Bouar, E., Obligis, E. and Ali-Mehenni, M.: The Rain Profiling Algorithm Applied to Polarimetric Weather Radar. J. Atmos. Oceanic Technol., 17: 332-356. http://dx.doi.org/10.1175/1520-0426(2000)017%3C0332:TRPAAT%3E2.0.CO;2, 2000.

Thurai, M., and Bringi, V.N.: Drop axis ratios from 2D video disdrometer. J. Atmos. Oceanic Technol., 22, 963–975.
510 https://doi.org/10.1175/JTECH1767.1, 2005.

Westrelin, S., Meriaux, P., Tabary, P., and Aubert Y.: Hydrometeorological risks in Mediterranean mountainous areas - RHYTMME Project: Risk Management based on a Radar Network. ERAD 2012 7th European Conference on Radar in Meteorology and Hydrology, June 2012, Toulouse, France. 6 p., hal-01511157, 2012.

515

Yu, N., Gaussiat, N., and Tabary, P.: Polarimetric X-band weather radars for quantitative precipitation estimation in mountainous regions. Q. J. Royal Meteorol. Soc., 144(717), DOI:10.1002/qj.3366, 2018.

Yu, N. and Gaussiat, N.: A monotonic algorithm for estimation of the specific differential phase. Poster presentation during
520 the 10th European Conference on Radar in Meteorology and Hydrology (ERAD 2018), 1-6 July 2018, Ede-Wageningen, The Netherlands, 2018.

	MOUC radar	XPORT radar
Longitude (decimal degrees)	5.639237	5.762327
Latitude (decimal degrees)	45.147736	45.194150
Altitude (m asl)	ground: 1901 antenna feedhorn: 1917	ground: 213 antenna feedhorn: 228
Frequency (GHz)	9.420	9.400
Antenna diameter (m)	1.8	1.8
3-dB beamwidth (°)	1.28	1.37
Antenna gain (dB)	42	42
Radome	yes	no
Peak power	30 kW, on each polarisation	50 kW, on each polarisation
Pulse length (µs)	2	1
Radial bin size (m)	240	33
Receiver dynamic range (dB)	>90	>90
Minimum detectable signal (dBm)	-114	-112
Volume scanning protocol (PPIs with elevation angles in °)	0 / 0.6 / 1.2 / 2 / 3 / 4 / 8 / 14°	3.5 / 7.5 / 15 / 25 / 45°
Volume scanning period (min)	5	~6
Measured parameters	$Z_h, Z_v, Z_{dr}, \rho_{hv}, \phi_{dp}, v_r$	

525 **Table 1. Characteristics of the XPORT and MOUC radar systems**
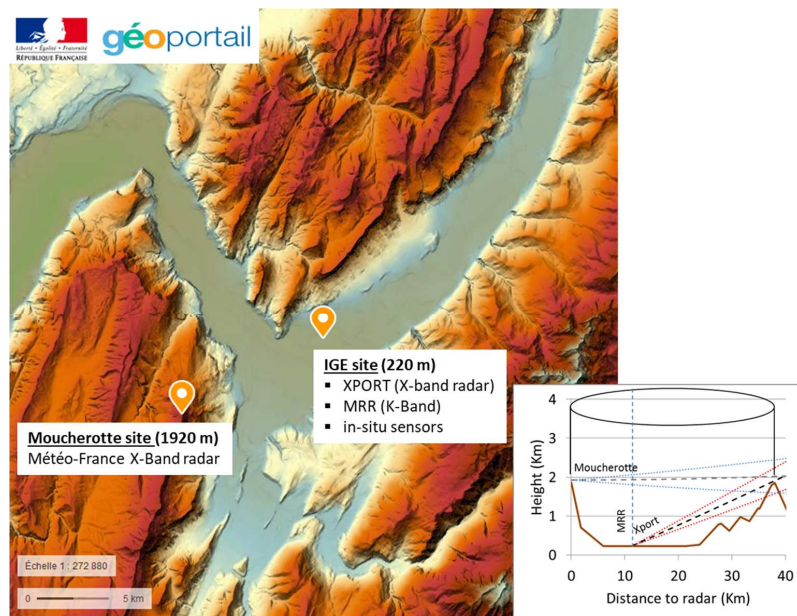
530

Figure 1. The topographical map of Grenoble is shown along with positions of two radar systems. A vertical cross-section along the line joining the two radar sites is shown in the insert on the bottom right of the figure.

535
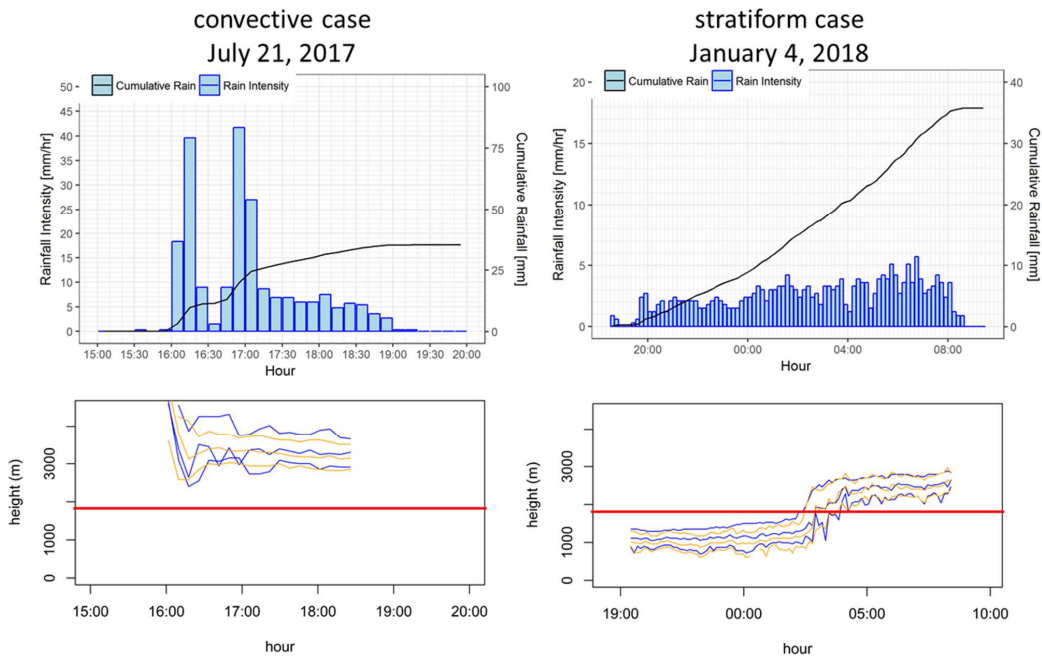
Figure 2. Description of the two rain events considered in the present study: left – convective case of July 21, 2017; right – stratiform case of January 4, 2018 ; top: rainrate and cumulative rainfall timeseries observed at the IGE site ; bottom:

540   results of the ML detection algorithm based on XPORT 25°-PPI data. The horizontal red line indicates the altitude of the MOUC radar; see text for details.
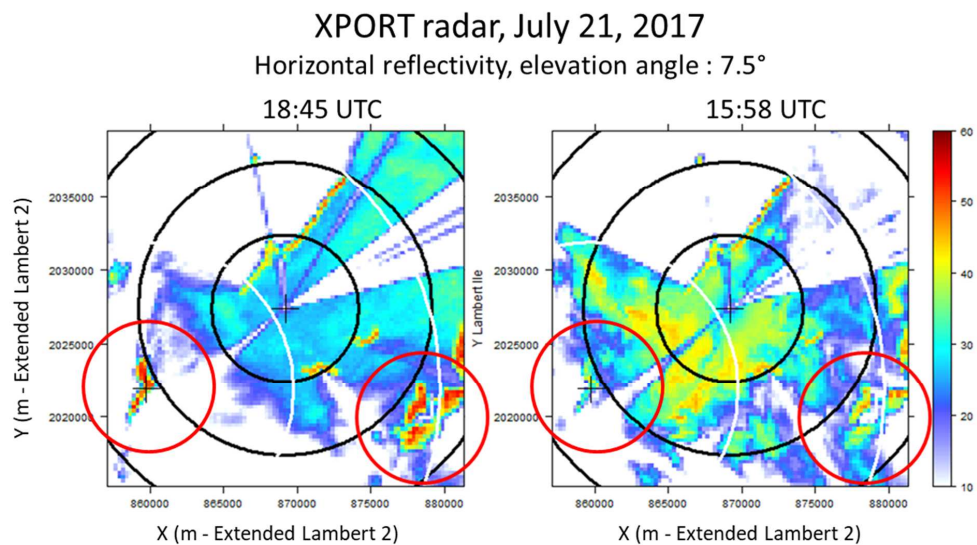
545   **Figure 3. Examples of XPORT 7.5° PPIs of raw reflectivity (non-corrected for attenuation) taken for two time steps during the July 21, 2017 convective event. The crosses indicate the location of the two radars and the black / white 5 / 10-km range markers correspond to the XPORT and the MOUC radar, respectively. The red circles focus the attention of the reader on the mountain returns associated with the Chamrousse (south-east) and the Moucherotte (south-west) mounts in between the 10-15 km range.**

550
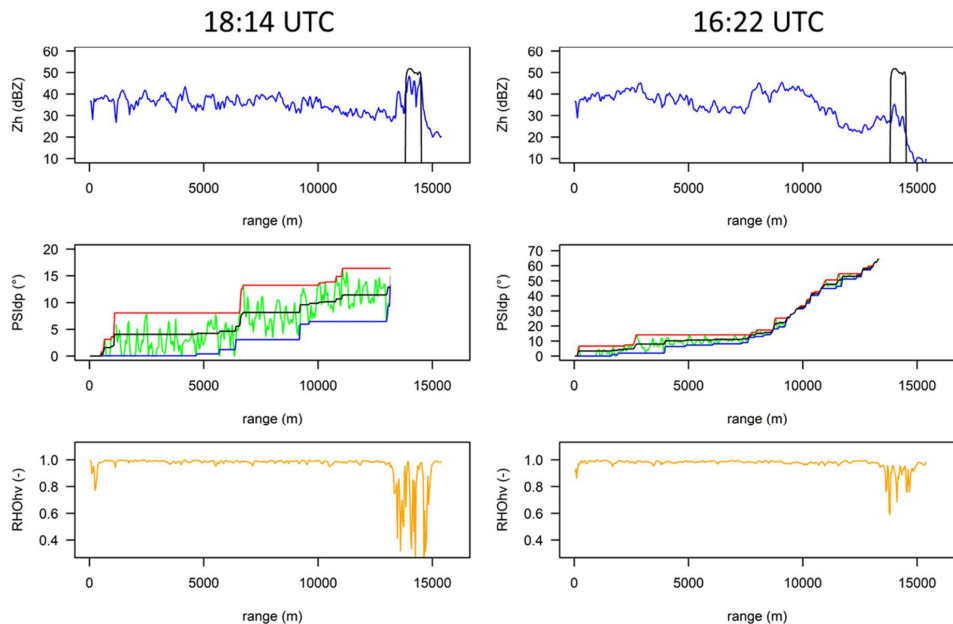
Figure 4. Two examples (left, right) of Z_h, ψ_{dp}, ρ_{hv} range profiles of the XPORT radar (7.5°-PPI) during the July 21, 2017
convective event for a given mountain target. The raw horizontal reflectivity profiles (top graphs) at the considered time
555   steps (blue) are displayed together with the dry-weather reference target value (black) at a range of about 14 km. The
middle graphs display the measured ψ_{dp} profiles (green), the upper (red) and lower (blue) envelope curves and the
regularized ψ_{dp} profiles (black). The ρ_{hv} profiles (bottom graphs) are used, together with the Z_h profiles, to detect the
rainy gates not affected by clutter at close range and in the region of the mountain target.

560
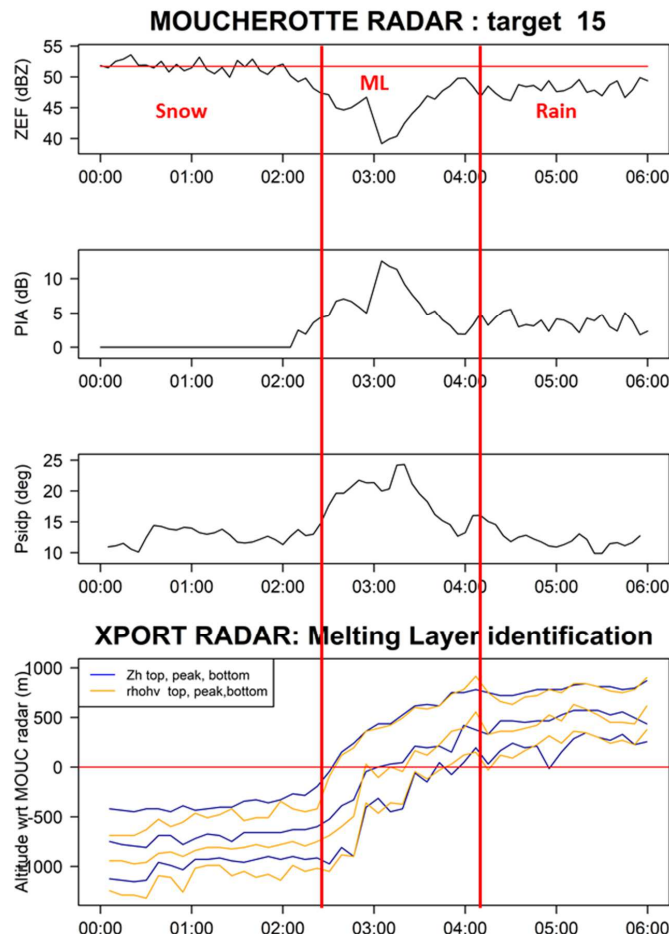
Figure 5. Timeseries of **(a)** the apparent reflectivity values of a given mountain reference target, **(b)** the resulting PIA estimates (dB), **(c)** the corresponding $\psi_{dp}(r_M)$ values (°) for the 0°-PPI of the MOUC radar during the January 3-4, 2018 stratiform rain event. The bottom graph **(d)** displays the results of the ML detection algorithm performed with the XPORT 565 25°-PPI; see text for details.
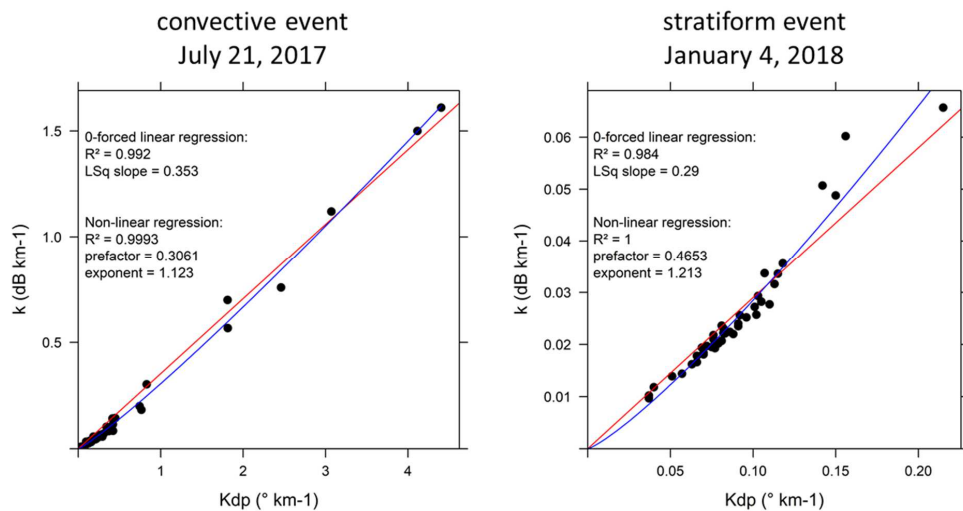
570   **Figure 6.** DSD-derived $k - K_{dp}$ relationships for the convective event of July 21th, 2017 (left) and for the stratiform event of January 3-4th, 2018; see text for details.

575
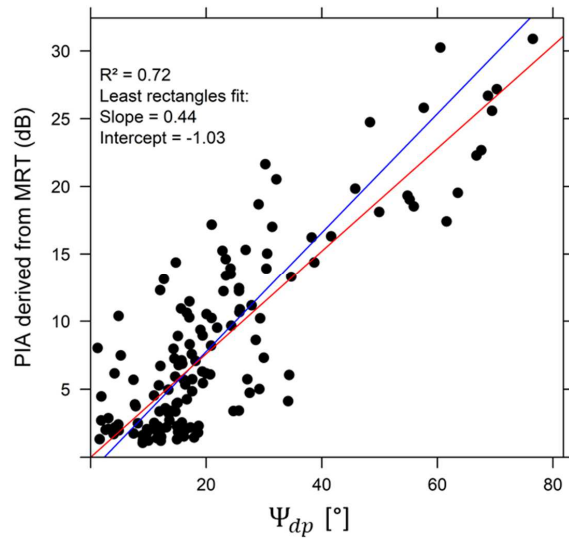
Figure 7. $\psi_{dp} - PIA$ **relationship in rain for the convective event of July 21**[th]**, 2017.**

580
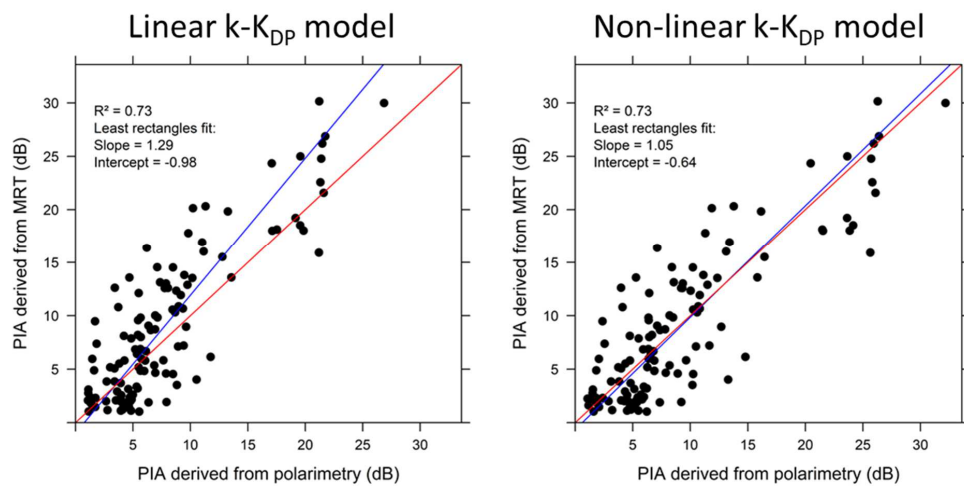
Figure 8. Comparison of the PIAs derived from the Mountain Reference Technique and from polarimetry using the linear k-K_{dp} relationship (left) and the non-linear k-K_{dp} relationship (right) for the convective event of July 21th, 2017. The red straight line is the 1/1 line.

585
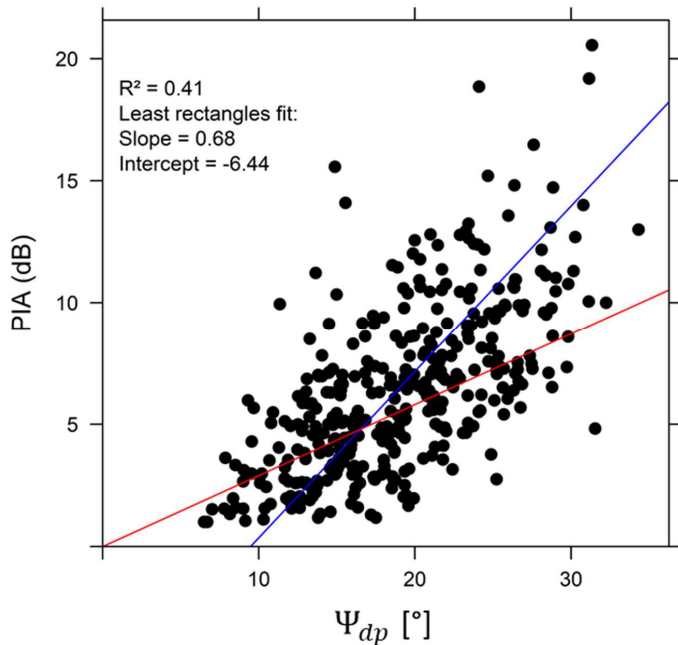
Figure 9. $\psi_{dp} - PIA$ **relationship in the ML for the stratiform event of January 4th, 2018.**

590
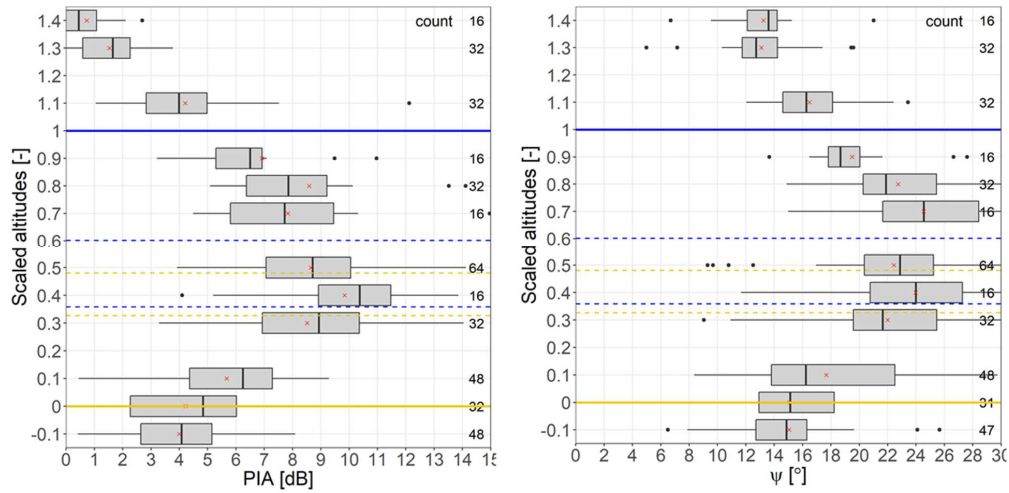
Figure 10. *PIA* and ψ_{dp} **values within the ML as a function of the scaled altitude (left and right, respectively) for the stratiform event of January 4th, 2018. The horizontal blue and orange continuous lines represent the ML top and bottom, respectively; the**

595   **dotted horizontal blue and orange lines give the 10 and 90% quantiles of the scaled altitudes of the Zh and ρ_{hv} peak distributions, respectively.**

600
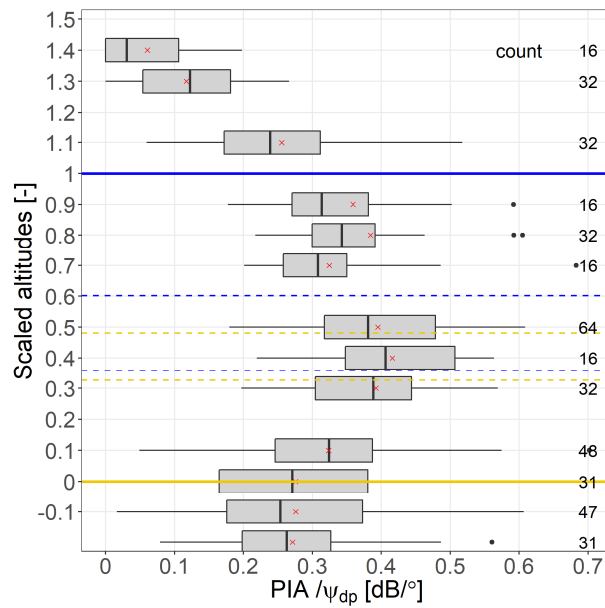
Figure 11. PIA/ψ_{dp} **values within the ML as a function of the scaled altitudes for the stratiform event of January 4th, 2018. The horizontal blue and orange lines represent the ML top and bottom, respectively; the dotted horizontal blue and orange lines give the 10 and 90% quantiles of the scaled altitudes of the Zh and ρ_{hv} peak distributions, respectively.**

605